CHIN. PHYS. LETT. Vol. 37, No. 8 (2020) 087101

de Haas–van Alphen Quantum Oscillations in $BaSn_3$ Superconductor with Multiple Dirac Fermions

Gaoning Zhang(张高宁)[1†], Xianbiao Shi(石贤彪)[2,3†], Xiaolei Liu(刘晓磊)[1†], Wei Xia(夏威)[1], Hao Su(苏豪)[1], Leiming Chen(陈雷明)[4], Xia Wang(王霞)[1,5], Na Yu(余娜)[1,5], Zhiqiang Zou(邹志强)[1,5], Weiwei Zhao(赵维巍)[2,3*], and Yanfeng Guo(郭艳峰)[1,6*]

[1]*School of Physical Science and Technology, ShanghaiTech University, Shanghai 201210, China*
[2]*State Key Laboratory of Advanced Welding & Joining and Flexible Printed Electronics Technology Center, Harbin Institute of Technology, Shenzhen 518055, China*
[3]*Key Laboratory of Micro-systems and Micro-structures Manufacturing of Ministry of Education, Harbin Institute of Technology, Harbin 150001, China*
[4]*School of Materials Science and Engineering, Henan Key Laboratory of Aeronautic Materials and Application Technology, Zhengzhou University of Aeronautics, Zhengzhou 450046, China*
[5]*Analytical Instrumentation Center, School of Physical Science and Technology, ShanghaiTech University, Shanghai 201210, China*
[6]*CAS Center for Excellence in Superconducting Electronics (CENSE), Chinese Academy of Sciences, Shanghai 200050, China*

(Received 26 May 2020; accepted 17 June 2020; published online 28 July 2020)

Characterization of Fermi surface of the $BaSn_3$ superconductor ($T_c \sim 4.4$ K) by de Haas–van Alphen (dHvA) effect measurement reveals its non-trivial topological properties. Analysis of non-zero Berry phase is supported by the *ab initio* calculations, which reveals a type-Ⅱ Dirac point setting and tilting along the high symmetric K–H line of the Brillouin zone, about 0.13 eV above the Fermi level, and other two type-I Dirac points on the high symmetric Γ–A direction, but slightly far below the Fermi level. The results demonstrate $BaSn_3$ as an excellent example hosting multiple Dirac fermions and an outstanding platform for studying the interplay between nontrivial topological states and superconductivity.

PACS: 71.18.+y, 74.70.Ad, 72.20.My, 74.25.−q DOI: 10.1088/0256-307X/37/8/087101

The nontrivial topological states in solids have brushed up our knowledge on band theory, which provide a platform to conveniently study the intriguing physics of some elementary particles with properties akin to those predicted in high-energy physics, such as Dirac fermions,[1–3] Weyl fermions,[4–7] Majorana fermions,[8–12] and even other exotic new fermions that have no counterparts in high-energy physics.[13–16] The realization of these particles in solids rather than in high-energy physics is owing to the numerous symmetries of solids and their versatile operations, which is somewhat difficult in high-energy physics. The different fermions usually require protection of different symmetries, for example, the four-fold Dirac point (DP) is protected by both time-reversal (TR) and space-inversion (SI) symmetries while the doubly degenerate Weyl points emerge in pair when any one or both of TR and SI symmetries are broken, so the combination of different fermions in a single material is definitely challenging but is rather attractive for the realization of multiple functionalities.

Recently, exploration of non-trivial topological states in superconductors has garnered increased attention,[8–12] because the interplay of non-trivial band topology and superconductivity may give rise to topological superconductivity hosting the long-pursuing Majorana fermion, which is potential for the use in low decoherence topological quantum computation.[17–20] The ASn_3 (A is an alkaline earth metal) superconductors have been scarcely studied, while the recent studies on $CaSn_3$ indicated it as a weakly coupled type-Ⅱ superconductor hosting eight pairs of WPs in the Brillouin zone (BZ) with closed loops of surface Fermi arcs.[21,22] Due to ionic radius mismatch between A and Sn ions, ASn_3 generally crystallizes in the variant structures of $AuCu_3$, for ex-

Supported by the National Natural Science Foundation of China (Grant No. 11874264), the Strategic Priority Research Program of Chinese Academy of Sciences (Grant No. XDA18000000), the Starting Grant of ShanghaiTech University, the Shenzhen Peacock Team Plan (Grant No. KQTD20170809110344233), the Bureau of Industry and Information Technology of Shenzhen through the Graphene Manufacturing Innovation Center (Grant No. 201901161514), the Key Scientific Research Projects of Higher Institutions in Henan Province (19A140018), and Analytical Instrumentation Center, SPST, ShanghaiTech University (Grant No. SPST-AIC10112914).
†Gaoning Zhang, Xianbiao Shi and Xiaolei Liu contributed equally to this work.
*Corresponding authors. Email: wzhao@hit.edu.cn; guoyf@shanghaitech.edu.cn

ample, $CaSn_3$ is in the $AuCu_3$-type structure while $BaSn_3$ ($T_c = 4.3$ K) has a hexagonal structure, seen in Fig. 1(a).[23] In light of the intriguing properties of $CaSn_3$, investigation on $BaSn_3$ in terms of the electronic structure is very valuable. By performing de Haas–van Alphen (dHvA) effect measurements and *ab initio* calculations, we have demonstrated herein that the $BaSn_3$ superconductor hosts multiple Dirac fermions.

High-quality $BaSn_3$ crystals were grown with a self-flux method. The Ba pieces and Sn lumps were mixed in the molar ratio 1 : 6 and sealed in an evacuated quartz tube under the vacuum of about 10^{-4} Pa. The tube was slowly heated to 700 ℃ in 15 h, kept at this temperature for 10 h and then slowly cooled down to 400 ℃ at a rate of 3 ℃/h. The single crystals were obtained by immediately putting the tube in a high-speed centrifugation at this temperature to remove the excess Sn. A typical crystal of $BaSn_3$ is shown on a millimeter grid by the inset of Fig. 1(c). The crystallographic phase and crystal quality were examined on a Bruker D8 single crystal x-ray diffractometer (SXRD) with Mo K_α ($\lambda = 0.71073$ Å) at 300 K, giving the space group $P6_3/mmc$ (No.194) with lattice parameters $a = b = 7.2424$ Å, $c = 5.4870$ Å, and $\alpha = \beta = 90°$, $\gamma = 120°$, consistent with the previous report.[23] The energy dispersive spectroscopy (EDS) characterizations revealed a good stoichiometry, as shown in Fig. 1(c). The high quality of the crystal is confirmed by the perfect reciprocal space lattice of SXRD without any other miscellaneous points, seen in Figs. 1(d)–(f). The electrical transport and magnetic measurements were separately performed on a physical property measurement system (PPMS) and a magnetic property measurement system (MPMS) from Quantum Design. Magnetic susceptibilities were measured with the magnetic field B of 10 Oe with B perpendicular to the (001) plane. The magnetic susceptibility of the $BaSn_3$ crystal is presented in Fig. 1(b) with the inset showing the temperature-dependent longitudinal resistivity ρ_{xx} measured with the electrical current $I = 50\,\mu$A along the c-axis. Both of them display an onset superconducting temperature $T_c^{\rm onset} \sim 4.4$ K, which are rather close to the values reported in the literature.[23] The B-dependent magnetization at 2 K is shown in the right inset of Fig. 1(b), exhibiting clear hysteresis that points to a type-Ⅱ superconductivity. Since Sn has a T_c of about 3.6 K with a type-I superconductor nature, different superconductivities of $BaSn_3$ and Sn exclude the possibility that the superconductivity of $BaSn_3$ is from the Sn flux rather than from the bulk.

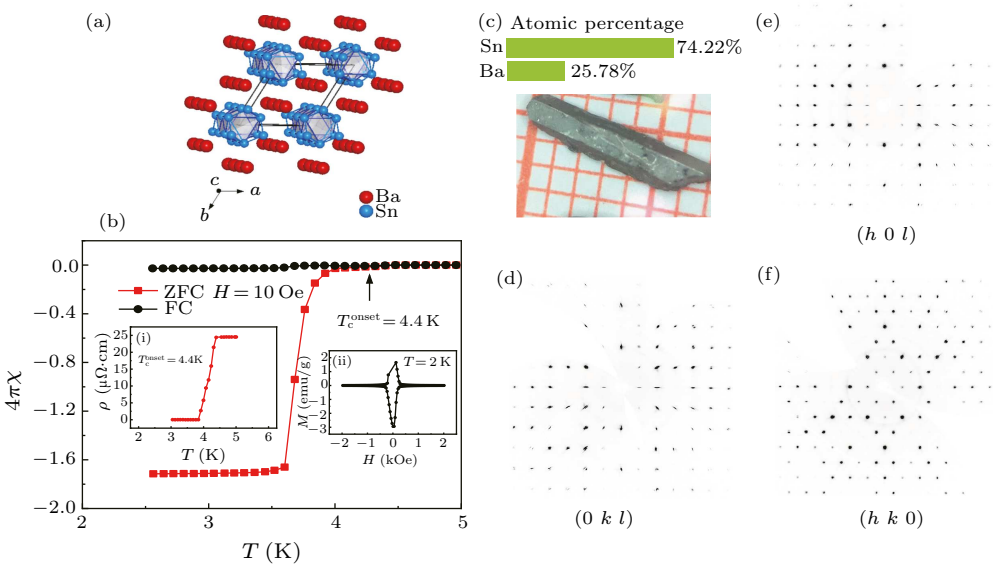

Fig. 1. (a) Schematic crystal structure of $BaSn_3$. (b) Temperature dependence of magnetic susceptibility. Insets: (i) the temperature-dependent resistivity of $BaSn_3$ at $B = 0$; (ii) the isothermal magnetization at 2 K. (c) The EDS result and a picture of a typical crystal for $BaSn_3$. (d)–(f) Diffraction patterns in the reciprocal space along the (0kl), (h0l), and (hk0) directions.

The first-principles calculations were carried out within the framework of the projector augmented wave (PAW) method,[24,25] by employing the generalized gradient approximation (GGA)[26] with the Perdew–Burke–Ernzerhof (PBE)[27] exchange-correlation functional, as implemented in the Vienna *ab initio* Simulation Package (VASP).[28–30] A kinetic energy cut-off of 500 eV and a Γ-centered k mesh of $6 \times 6 \times 9$ were utilized in all calculations. The energy and force difference criterion were defined as 10^{-6} eV and 0.01 eV/Å for self-consistent convergence and structural relaxation, respectively. The WANNIER90 package[31–33] was adopted to construct Wannier functions from the first-principles results

without an iterative maximal-localization procedure. The WANNIERTOOLS[34] code was used to investigate the topological features of surface state spectra.

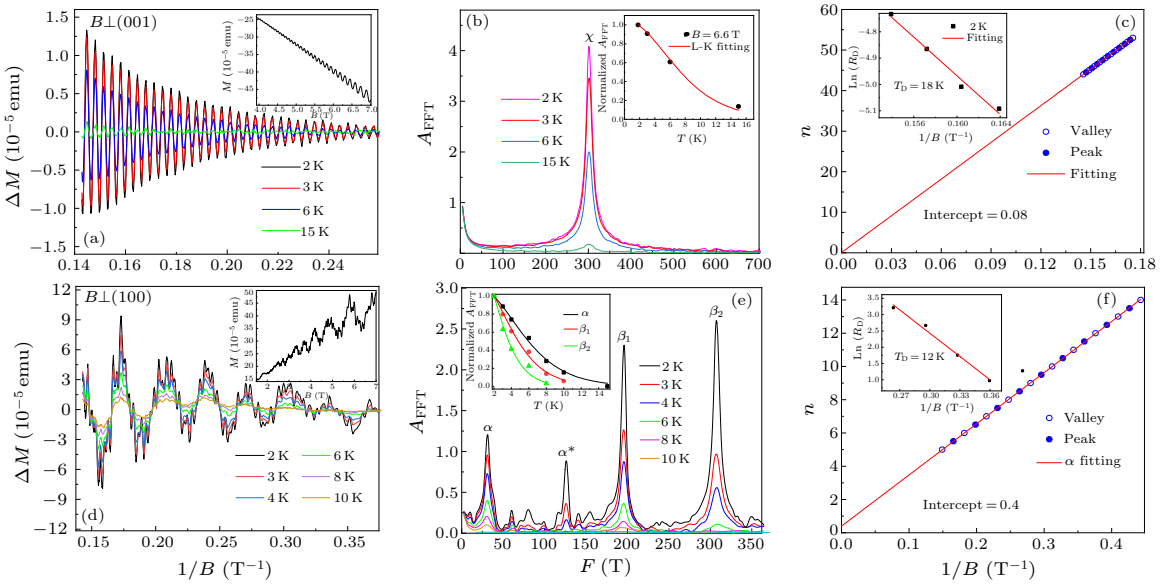

Fig. 2. (a) and (d) Quantum oscillations for $BaSn_3$ with $B\perp(001)$ and (100) at various temperatures. Each corresponding inset shows the raw magnetization at 2 K. (b) and (e) Temperature dependence of FFT spectra. The corresponding insets show the LK fitting to the oscillation amplitudes. (c) and (f) The Landau level fan diagrams for the fundamental frequencies of χ and α, respectively. The corresponding insets show the Dingle fitting results.

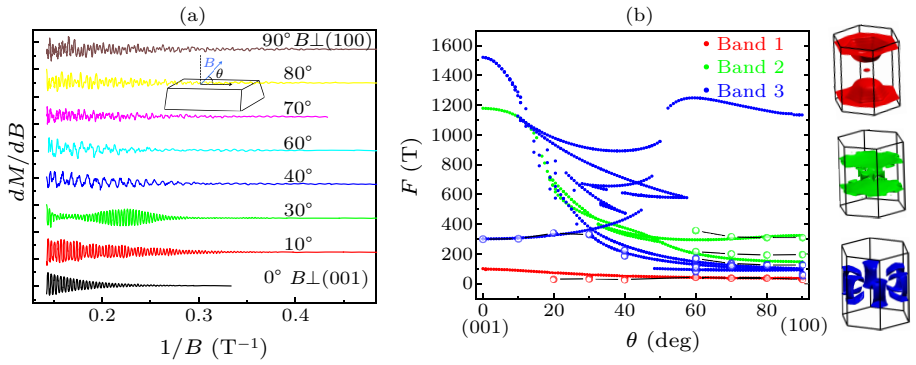

Fig. 3. (a) First-order differential of dHvA oscillatory at $T = 2$ K for both $B\perp(100)$ and (001) of $BaSn_3$. Inset: the schematic measurement configuration. (b) Quantum oscillatory frequencies vs θ. The solid dots depict the calculation results and the color circles represent the experimental values. The red circles correspond to α, the green circles correspond to β_1 and β_2 (band 2), and the blue circles represent χ (band 3). The corresponding FSs within the hexagonal first Brillouin zone are shown on the right.

Seen in Figs. 2(a) and 2(d), clear dHvA quantum oscillations in the isothermal magnetizations starting from $B = 2$ T in the temperature range of 2–15 K are visible when B is perpendicular to both (001) and (100) planes. In Figs. 2(a) and 2(d), we present the oscillatory components of magnetization for $BaSn_3$ at different temperatures, which were obtained after subtracting the background, i.e., $\Delta M = M - M_{\text{background}}$. In general, the quantum oscillations could be well described by the Lifshitz–Kosevich (LK) formula:[35]

$$\Delta M \propto -B^{\lambda} R_{\text{T}} R_{\text{D}} R_{\text{s}} \sin\left[2\pi\left(\frac{F}{B} - \gamma - \delta\right)\right],$$

where $R_{\text{T}} = \alpha T\mu/B\sinh(\alpha T\mu/B)$ with μ being the ratio of effective cyclotron mass m^* to free electron mass m_0 and $\alpha = (2\pi^2 k_{\text{B}} m_0)/(\hbar e)$, $R_{\text{D}} = \exp(-\alpha T_{\text{D}}\mu/B)$ with T_{D} being the sample-dependent Dingle temperature, and $R_{\text{s}} = \cos(\pi g\mu/2)$. The exponent λ is determined by the dimensionality, where $\lambda = 1/2$ and 0 are for the three-dimensional (3D) and 2D cases, respectively. The oscillation part is described by the sine term with a phase factor $-\gamma - \delta$, in which $\gamma = \frac{1}{2} - \frac{\Phi_{\text{B}}}{2\pi}$ with Φ_{B} being the Berry phase. The phase shift is determined by the dimensionality of the FS and takes a value of 0 for 2D and $\pm 1/8$ ($-$ for the electron-like pocket and $+$ for the hole-like pocket) for the 3D case.[36] The fast Fourier transform (FFT) analysis of dHvA oscillations are depicted in Figs. 2(b) and 2(e) after the first-order differential of the M vs $1/B$. A single frequency labeled

as $\chi = 300.8\,\mathrm{T}$ was obtained from the analysis on the oscillations when $B\perp(001)$, corresponding to the calculated band 3 in Fig. 3(b). Multiple frequencies associated with the oscillations when $B\perp(100)$ were obtained in the FFT spectra as shown in Fig. 2(e). In order to achieve more accurate fits, we separated the low- and high-frequency components with band-pass filtering and fitted them individually. The multiple frequencies in the FFT spectra indicate the presence of multiple Fermi pockets around the Fermi energy level E_F. Moreover, the anisotropic dHvA oscillations presented in Fig. 3(a) confirm the 3D nature of the FS in $BaSn_3$. From the temperature-dependent FFT spectra, four main frequencies for $B\perp(100)$ could be identified, labeled as α (31.5 T), α^* (126 T), β_1 (196.6 T), β_2 (306.7 T), where $\alpha^* = 4\alpha$ is the harmonic value of α. The angle-dependent frequencies α, β_1, and β_2 are comparable to those calculated for bands 1 and 2, respectively, as shown in Fig. 3(b). The area of FS can be determined by the Onsager relation $F = A_\mathrm{F}(\varphi/2\pi^2)$, where $\varphi = h/2e$ is the magnetic flux and A_F is the FS area. The derived parameters are summarized in Table 1. The effective mass m^* can be obtained by fitting the temperature-dependent oscillation amplitude to the thermal damping factor R_T, as shown by the insets in Figs. 3(b) and 3(e). For all the obtained oscillation frequencies, the effective masses are estimated to be $0.135m_0$–$0.29m_0$, which are very close to the DFT calculated values, $0.1m_0$–$0.3m_0$. Fitting to the field dependent amplitudes of the quantum oscillations at 2 K, as shown in Figs. 2(c) and 2(f), gives the Dingle temperatures $T_\mathrm{D} = 12\,\mathrm{K}$ and 18 K for bands α and χ, respectively.

The Landau level (LL) index fan diagram is constructed, aiming at examination of the Berry phase of $BaSn_3$ accumulated along the cyclotron orbit.[37] The LL index phase diagrams of α and χ are shown in Figs. 2(c) and 2(f), respectively, in which the valley positions of dM/dB against $1/B$ were assigned to be integer indices and the peak positions were assigned to be half-integer indices. A good linear fitting gives the intercepts of 0.4, −0.04, −0.35, and 0.08 corresponding to α, β_1, β_2, and χ, respectively. The derived Berry phases Φ_B are $(0.8 + 0.25)\pi$, $(-0.08 + 0.25)\pi$, $(-0.7 + 0.25)\pi$ and (0.16–0.25)π for the hole pockets α, β_1, β_2 and the electronic pocket χ. The band-pass filtering was changed in different ranges and the error bars for the fitted Barry phases for α, β_1, β_2, and χ are in the range of 0.04π–0.1π. The Berry phases for the α frequency is close to π, implying the nontrivial type-Ⅱ Dirac point in band 1, while the hole band β_1 and electronic band χ are topologically trivial. We also calculated that the type-I related the band 2, but the high Landau level index may cause the frequency β_2 deviation. The results are supported by the theoretical calculations presented later. All derived parameters are summarized in Table 1.

Table 1. Parameters derived from dHvA oscillations for $BaSn_3$. Here k_F is the Fermi wave vector, ν_F denotes the Fermi velocity, μ^* represents the carrier mobility, τ is the relaxation time, and Φ_B is the Berry phase.

	F (T)	A_F (nm^{-2})	k_F (nm^{-1})	ν_F (m/s)	E_F (meV)	m^*/m_0	T_D (K)	τ (s)	μ^* (cm^2/Vs)	Φ_B
$B\perp(100)$	31.5	0.3	0.31	2.6×10^5	54	0.135	12	1×10^{-13}	1302	$1.05(\delta=+1/8)$
	196.6	1.87	0.77	5.03×10^5	258	0.178	3	4×10^{-13}	3951	$0.17(\delta=+1/8)$
	306.7	2.93	0.97	3.86×10^5	248	0.29	2.2	5.5×10^{-13}	3307	$-0.45(\delta=+1/8)$
$B\perp(001)$	300.8	2.87	0.96	8.03×10^5	509	0.138	18	6.7×10^{-13}	849	$-0.09(\delta=-1/8)$

The band structure of $BaSn_3$ in the absence of spin–orbit coupling (SOC) is shown in Fig. 4(a), revealing a metallic behavior with several bands crossing the E_F and the multi-band nature of the superconductivity. When SOC is taken into account, we focus our special attention on the bands near the E_F along the Γ–A and K–H high symmetry lines. Along the Γ–A direction, as seen in Fig. 4(b), the lowest conduction band at the Γ point with Γ_7^- irreducible representation (IR) shows a linearly downward dispersion and crosses with the first and second highest valence bands which belong to Γ_9^- and Γ_8^+ IRs, respectively. The two unavoidable band crossing points due to the different IRs of relevant bands, see in Fig. 4(b), are labeled by red and blue filled circles and donated as DP1 and DP2, respectively. Due to protection by both TR and SI symmetries, each band in $BaSn_3$ is doubly degenerate, thus making DP1 and DP2 the actually four-fold degenerate type-I DPs. Figures 4(c) and 4(d) present the band structure in the k_x–k_y plane surrounding DP1 and DP2, in which the band dispersion around both DP1 and DP2 is actually anisotropic, consistent with our above analysis on the dHvA oscillations. In Fig. 4(e), we show the electronic bands along the K–H direction, supporting the presence of type-Ⅱ Dirac point, which is labeled by a green filled circle and donated as DP3. Similarly, symmetry analysis shows that the DP3 is also unavoidable because of the crossing bands belonging to different IRs (Λ_4 and Λ_{5+6}). The Dirac cone tilts strongly along the K–H direction, whereas does not tilt in the k_x–k_y plane, seen in Fig. 4(f). Figure 4(g) shows the schematic position of all the DPs in the BZ.

The (001) surface band structure is presented in Fig. 4(h), on which the bulk DP1 and DP2 located on the k_z axis are projected onto the surface $\bar{\Gamma}$ point

and hidden in the continuous bulk states. The surface states indicated by green arrows around the $\bar{\Gamma}$ point stemming from the projections of the bulk DP1 and DP2 are only partially observed. These topological states are far below the $E_{\rm F}$, they consequently will not play a role in the measured transport properties, similar to the situation occurring in type-Ⅱ DSMs $PdTe_2$ and $PtSe_2$.[37,38] In the case of DP3 that distributed on the K–H line, it is projected onto the surface $\bar{K}$ point. Though DP3 is 0.13 eV above the $E_{\rm F}$, the surface state emanates from the projections of DP3 passing through the $E_{\rm F}$ around the $\bar{K}$ point. This will contribute to the transport properties and help us to understand the measured quantum oscillations in $BaSn_3$.

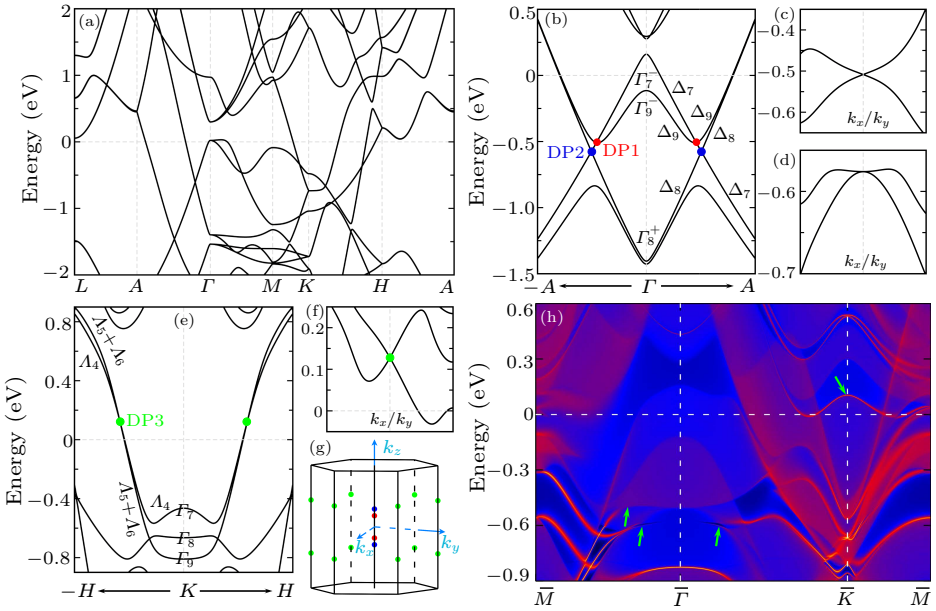

Fig. 4. (a) The calculated band structure of $BaSn_3$ without SOC. (b) Energy dispersion along the Γ–A line with SOC, displaying two pairs of DPs. The irreducible representations of selected bands along the high-symmetric k are indicated. (c) and (d) Band structures in the k_x–k_y plane surrounding the DP1 and DP2 in (b). (e) The same as (b) but along the K–H line, showing a pair of DPs. (f) Band structure in the k_x–k_y plane in the vicinity of DP3 in (e). (g) Schematic position of the DPs in the BZ. (h) Topological surface states of $BaSn_3$ on the (001) surface. The green arrows mark surface states around the projected DPs.

In summary, the dHvA quantum oscillations and first-principle calculations have demonstrated the type-I and type-Ⅱ Dirac fermions in $BaSn_3$ superconductor, which makes $BaSn_3$ an excellent platform for the study of novel topological physics and exploring multiple functionalities. Moreover, since $BaSn_3$ is an intrinsic superconductor with non-trivial topological states, it would be very interesting to explore topological superconductivity which may be produced by the interplay between the two states. This holds a possibility for making $BaSn_3$ more attractive in topological applications.

References

[1] Young S M, Zaheer S, Teo J C Y, Kane C L, Mele E J and Rappe A M 2012 *Phys. Rev. Lett.* **108** 140405

[2] Wang Z, Sun Y, Chen X Q, Franchini C, Xu G, Weng H, Dai X and Fang Z 2012 *Phys. Rev. B* **85** 195320

[3] Liu Z K, Zhou B, Zhang Y, Wang Z J, Weng H M, Prabhakaran D, Mo S K, Shen Z X, Fang Z, Dai X, Hussain Z and Chen Y L 2014 *Science* **343** 864

[4] Lv B Q, Weng H M, Fu B B, Wang X P, Miao H, Ma J, Richard P, Huang X C, Zhao L X, Chen G F, Fang Z, Dai X, Qian T and Ding H 2015 *Phys. Rev. X* **5** 031013

[5] Weng H, Fang C, Fang Z, Bernevig B A and Dai X 2015 *Phys. Rev. X* **5** 011029

[6] Yang L X, Liu Z K, Sun Y, Peng H, Yang H F, Zhang T, Zhou B, Zhang Y, Guo Y F, Rahn M, Prabhakaran D, Hussain Z, Mo S K, Felser C, Yan B and Chen Y L 2015 *Nat. Phys.* **11** 728

[7] Xu S Y, Belopolski I, Alidoust N, Neupane M, Bian G, Zhang C, Sankar R, Chang G, Yuan Z, Lee C C, Huang S M, Zheng H, Ma J, Sanchez D S, Wang B, Bansil A, Chou F, Shibayev P P, Lin H, Jia S and Hasan M Z 2015 *Science* **349** 613

[8] Fu L and Kane C L 2008 *Phys. Rev. Lett.* **100** 096407

[9] Xu J P, Wang M X, Liu Z L, Ge J F, Yang X, Liu C, Xu Z A, Guan D, Gao C L, Qian D, Liu Y, Wang Q H, Zhang F C, Xue Q K and Jia J F 2015 *Phys. Rev. Lett.* **114** 017001

[10] Zhang P, Yaji K, Hashimoto T, Ota Y, Kondo T, Okazaki K, Wang Z, Wen J, Gu G D, Ding H and Shin S 2018 *Science* **360** 182

[11] Wang D, Kong L, Fan P, Chen H, Zhu S, Liu W, Cao L, Sun Y, Du S, Schneeloch J, Zhong R, Gu G, Fu L, Ding H and Gao H J 2018 *Science* **362** 333

[12] Liu Q, Chen C, Zhang T, Peng R, Yan Y J, Wen C H P, Lou X, Huang Y L, Tian J P, Dong X L, Wang G W, Bao W C, Wang Q H, Yin Z P, Zhao Z X and Feng D L 2018 *Phys. Rev. X* **8** 041056

[13] Bradlyn B, Cano J, Wang Z, Vergniory M G, Felser C, Cava

R J and Bernevig B A 2016 *Science* **353** aaf5037
[14] Tang P, Zhou Q and Zhang S C 2017 *Phys. Rev. Lett.* **119** 206402
[15] Chang G, Xu S Y, Wieder B J, Sanchez D S, Huang S M, Belopolski I, Chang T R, Zhang S, Bansil A, Lin H and Hasan M Z 2017 *Phys. Rev. Lett.* **119** 206401
[16] Rao Z, Li H, Zhang T, Tian S, Li C, Fu B, Tang C, Wang L, Li Z, Fan W, Li J, Huang Y, Liu Z, Long Y, Fang C, Weng H, Shi Y, Lei H, Sun Y, Qian T and Ding H 2019 *Nature* **567** 496
[17] Wilczek F 2009 *Nat. Phys.* **5** 614
[18] Stern A 2010 *Nature* **464** 187
[19] Qi X L and Zhang S C 2011 *Rev. Mod. Phys.* **83** 1057
[20] Leijnse M and Flensberg K 2012 *Semicond. Sci. Technol.* **27** 124003
[21] Luo X, Shao D F, Pei Q L, Song J Y, Hu L, Han Y Y, Zhu X B, Song W H, Lu W J and Sun Y P 2015 *J. Mater. Chem. C* **3** 11432
[22] Zhu Y L, Hu J, Womack F N, Graf D, Wang Y, Adams P W and Mao Z Q 2019 *J. Phys.: Condens. Matter* **31** 245703
[23] Fässler T F and Kronseder C 1997 *Angew. Chem. Int. Ed. Engl.* **36** 2683
[24] Blöchl P E 1994 *Phys. Rev. B* **50** 17953
[25] Lehtomäki J, Makkonen I, Caro M A, Harju A and Lopez-Acevedo O 2014 *J. Chem. Phys.* **141** 234102
[26] Perdew J P, Burke K and Ernzerhof M 1996 *Phys. Rev. Lett.* **77** 3865
[27] Perdew J P and Wang Y 1992 *Phys. Rev. B* **45** 13244
[28] Kresse G and Furthmüller J 1996 *Phys. Rev. B* **54** 11169
[29] Kresse G and Hafner J 1993 *Phys. Rev. B* **47** 558
[30] Kresse G and Furthmüller J 1996 *Comput. Mater. Sci.* **6** 15
[31] Mostofi A A, Yates J R, Lee Y S, Souza I, Vanderbilt D and Marzari N 2008 *Comput. Phys. Commun.* **178** 685
[32] Souza I, Marzari N and Vanderbilt D 2001 *Phys. Rev. B* **65** 035109
[33] Marzari N and Vanderbilt D 1997 *Phys. Rev. B* **56** 12847
[34] Wu Q S, Zhang S N, Song H F, Troyer M and Soluyanov A A 2018 *Comput. Phys. Commun.* **224** 405
[35] Mikitik G P and Sharlai Y V 1999 *Phys. Rev. Lett.* **82** 2147
[36] Hu J, Tang Z, Liu J, Liu X, Zhu Y, Graf D, Myhro K, Tran S, Lau C N, Wei J and Mao Z 2016 *Phys. Rev. Lett.* **117** 016602
[37] Clark O J, Neat M J, Okawa K, Bawden L, Marković I, Mazzola F, Feng J, Sunko V, Riley J M, Meevasana W, Fujii J, Vobornik I, Kim T K, Hoesch M, Sasagawa T, Wahl P, Bahramy M S and King P D C 2018 *Phys. Rev. Lett.* **120** 156401
[38] Yang H, Schmidt M, Süss V, Chan M, Balakirev F F, McDonald R D, Parkin S S P, Felser C, Yan B and Moll P J W 2018 *New J. Phys.* **20** 043008